

## The Radio Fundamental Catalogue. I. Astrometry

LEONID PETROV<sup>1</sup> AND Y. Y. KOVALEV<sup>2,3,4</sup>

<sup>1</sup>*NASA Goddard Space Flight Center*

*Code 61A1, 8800 Greenbelt Rd, Greenbelt, 20771 MD, USA*

<sup>2</sup>*Astro Space Center of Lebedev Physical Institute, Profsoyuznaya 84/32, 117997 Moscow, Russia*

<sup>3</sup>*Moscow Institute of Physics and Technology, Institutsky per. 9, Dolgoprudny, Moscow region, 141700, Russia*

<sup>4</sup>*Max-Planck-Institut für Radioastronomie, Auf dem Hügel 69, 53121 Bonn, Germany*

Submitted to AJ

### ABSTRACT

**We present . . .**

*Keywords:* Astrometry

### 1. INTRODUCTION

The method very long baseline interferometry (VLBI), first proposed by Matveenko et al. (1965) allows us to determine positions or compact radio sources with a nanoradian level of accuracy ( $(1 \text{ nrad} \approx 0.2 \text{ mas})$ ). The very first VLBI catalogue contained coordinates of 35 objects (Cohen & Shaffer 1971). Since then VLBI observations became routine for geodesy and astrophysics, and absolute astrometry programs. Initially, the geodesy VLBI program observed 14 bright sources. With an improvement of sensitivity or radio telescopes, a need for larger pool of geodetic sources emerged and first dedicated astrometric VLBI programs commenced Fanselow et al. (1984); Morabito et al. (1986); Preston et al. (1985). Analysis of all observations available by 1996 resulted in the ICRF catalogue of 608 sources (Ma et al. 1998).

These observations fulfilled the original goal and the list of geodetic sources grew to several hundreds. Approximately at the same time, in mid 1990s, the Very Long Baseline Array (VLBA) started to operate. The widely used mode of observation with VLBA is the phase-referencing or nodding mode when all antennas of the array are quickly switch from a target source to a calibrator within several degrees. Usually, the target is weaker than the calibrator. This observations allows to overcome the coherence limit set by atmospheric fluctuations and detect weaker sources by extending integration time. The atmospheric errors are diluted roughly by the angular distance between the target and calibrator expressed in radians. The closer the calibrator to the target, the better atmospheric errors are compensated. Martí-Vidal et al. (2010) has characterized quantitatively the impact of residual errors quality of results as a function of target to calibrator separation. In general a target to calibration separation less than  $2^\circ$  is desirable, separation  $2\text{--}5^\circ$  is unfavorable, and separation greater  $5^\circ$  should be avoided. Not every source is suitable as a calibrator. It should be compact to be detected at all baselines and bright for being scheduled for short integration time.

Phase calibration is used not only for imaging of weak sources, but also for differential astrometry. Accuracy at tens microarcseconds can be achieved for the *position offsets* when observed in a phase referencing mode (Reid & Honma 2014; Reid et al. 2017). Similar technique is also applicable to observations of spacecrafts (Jones et al. 2020). It should be noted that although differential phase referencing VLBI allows to evaluate position offsets with respect to a calibrator with very high precision, the position accuracy of a target source cannot be greater than the position accuracy of a calibrator, which may be orders of magnitude worse.

Detection of a large number of sources allows us to study a population of compact objects with compact emission that are almost exclusively active galactic nuclei (AGN) as a whole. Not all AGNs are compact enough to be detected

with VLBI at baselines longer 100 km. Correlating milliarcsecond-scale morphology of detected sources with the arcsecond-scale morphologies, spectral indices, and variability, provides rich information about the AGNs and is a key to for understanding their nature.

Bright compact radio sources are relatively rare objects. Knowing their statistics, the probability to find by a chance a compact AGN with certain flux density within a specified search area from a given direction can be evaluated. This probability is often small enough to draw an important conclusion that the objects found in that specified search area are statistically related. This approach was successfully used for association of  $\gamma$ -ray sources detected with *Fermi* space telescope with AGNs (Petrov et al. 2013; Schinzel et al. 2015, 2017; Ajello et al. 2020). **Zdes' nado napisat' pro neutrino**

Corr 1

These challenges articulated a necessity to derive a dense grid of a large number of calibrator sources that would make phase referencing observations feasible. Monte Carlo simulation showed that we need to have 6710 calibrator sources uniformly distributed over the celestial sphere in order to find a calibrator within  $3^\circ$  of a given direction with the probability of 99%. This number raises to 15100 if a calibrator within  $2^\circ$  of a given direction has to be found with that confidence level. Various applications have different requirements. Phase referencing observations for imaging require a large pool of calibrators with known images, but with medium positional accuracy (3–10 mas). Parallax measurements require position accuracy better than 3 mas. Space navigation requires high position accuracy 0.1 mas and better. It is impossible to satisfy all these requirements at once given limited amount of resources.

The activity to build this grid started in 1994 with the VLBA Calibrator Survey–1 Beasley et al. (2002) and is still on-going. It was quickly became clear that dedicated absolute astrometry observing campaigns need be organized to achieve the goals. At the time some suitable VLBI observations beyond those designed for absolute astrometry could contribute to the goal and they were accounted as well. In the context of the present article expression absolute astrometry is used in a sense of non-differential astrometry, i.e. deriving position of target sources without the a priori knowledge of positions of other sources. A more detailed explanation is provided in section 4.4.

Although the VLBI technique evolved since its conception, the basic approach for deriving the source catalogue remained intact since 1980s. VLBI data analysis is performed in a cumulative mode. That means that the latest VLBI astrometric solution uses all the data accumulated from the first observing session to the last. Each new solution supersedes the previous one. The number of sources is growing, blunders in previous solutions are corrected, and as a result position accuracy is improved, except rare cases when an unnoticed blunder in analysis might degrade quality of a solution. Therefore, any new solution is considered better than the previous one. This accumulative approach results in an evolutionary steady improvement in the output catalogue.

Historically, two groups developed accumulative VLBI source position catalogues. The ICRF working group produced new catalogues once per decade and used a limited number of observing campaigns. The Radio Fundamental Catalogue (RFC) working group releases a new catalogue on a quarterly basis and posted them online at <http://astrogeo.org/rfc> since February 09, 2009 and used all publicly available campaigns. Due to this approach the catalogue development is permanently in the development state and by the moment of writing 47 quarterly releases was made. This catalogue is widely used for scheduling and analysis of VLBI observations – nowadays over 2/3 VLBA observations use phase calibration, for association of high energy objects with AGNs, and for a number of other applications. We do not anticipate we will be in a position to declare that all work for deriving the catalogue is finished in at least three more years. Therefore, we present the RFC as is by 2021.07.01 as a data release one. We plan to provide on-line releases on a quarterly basis and we plan to publish updates in the future with a cadence of several years.

We split the material in paper I and paper II. The scope of paper I is description of observing campaigns, data analysis technique, global parameter estimation, error analysis of positions, technique for handling multiple sources and presentation of the source position catalogue. The scope of paper II is **Yura tvoj konyok**.

Corr 2

## 2. OBSERVING CAMPAIGNS

VLBI observations are organized in campaigns that can contain one or more segments also called experiments. A target source or several target sources, as well as several calibrator sources, are observed for 1–12 hours in a typical astronomical VLBI experiment. A goal of such a dedicated experiment is to observe either a single source of interest or a small group of sources (less than ten objects). Such sources are studied in detail at full sensitivity that is achieved for long integration time. This allows to reconstruct high fidelity images and/or get highly accurate source positions using differential VLBI. In contrast, tens to hundreds sources are observed in a given survey experiment, and a VLBI survey campaign may involve observations of several thousand sources. The goal of survey experiments is to study

a population of sources. Inevitably, shorter integration time us used in survey experiments. That results in poorer images and worse position accuracy than in dedicated experiments, but a much larger number of objects is observed.

Most of the surveys fall into three categories: pathfinder surveys, follow-up surveys, and high-frequency extensions. The goal of pathfinder VLBI surveys is to detect target sources never observed with VLBI before, to determine their positions at a milliarcsecond level of accuracy, and to reconstruct their images. Since VLBI has a small field of view, typically in a range of  $10''$  to  $5'$  at 2–24 GHz, a blind surveys would be very inefficient, because the probability to find a source with flux density 10–100 mJy within such a narrow field of view by chance is low. Therefore, target sources in pathfinder surveys are selected among those detected in prior connected radio interferometers at resolutions 1–40'' or single dish observations at resolutions 0.5'–5'. VLBI observations just follow up objects already detected at low resolutions. Only a fraction of target sources is detected with VLBI pathfinder survey. Depending on the criteria used for source selection, the fraction of detected sources is in a range of 5 to 98% with 59% being the median fraction.

The follow-up VLBI surveys target samples of the sources previously detected in prior VLBI pathfinder surveys with the goal to improve position accuracy or get a higher quality images. The radiotelescope sensitivity is usually the highest in a range of 1–9 GHz, and source flux density is usually falling with frequency. Therefore, chances to detect a source using given integration time are in general higher at lower frequencies. Sources detected at low frequencies are often followed-up at higher frequencies in the third type of surveys, called high-frequency extensions. The goal of these extensions is to get images of the sources at higher frequencies that better characterize the core region, evaluate the suitability of source as a calibrator at high frequencies, and in some cases to improve position accuracy.

In our work we collected data from all VLBI surveys for which we could find visibilities in public archives. This includes all surveys that we designed ourselves or participated as co-investigators, and all surveys found in literature. We combed through VLBA and EVN surveys and examined observing campaigns in continuum at frequencies above 4 GHz that observed target sources without the use of phase calibrators. In addition, we included all geodetic VLBI data since April 1980 as an auxiliary dataset. Although these data had only marginal direct impact on source position, their use significantly improved estimates of station positions and the Earth Orientation Parameters (EOP) that are nuisance parameters in the context of this work, but are essential for reducing systematic errors due to stability of the VLBI network and its motion with respect to the origin of the coordinate system.

Radio wave propagation is described by differential equations against source coordinates and other variables. Their solution require three initial conditions that define the orientation of the celestial coordinate system as well as initial conditions that define the origin and orientation of the terrestrial coordinate system. These initial conditions are arbitrary and cannot be determined from observations in principle. When positions of all sources from all campaigns are derived in a single least square (LSQ) solution, there are three free parameters. This can be done when there is an overlap between observing stations and observed sources between different campaigns. In an extreme case when two campaigns used different networks and different source lists without a common station and common source, and determined Earth Orientation Parameters (EOP) independently, for their processing in a single LSQ solution three additional arbitrary parameters have be used that describe rotations of the source positions between two campaigns. Such a solution would have little value. To avoid this situation, source lists in observing campaigns have a significant overlap by design. In addition to avoiding degeneracies in estimation of source coordinates, sources are observed in different campaigns to improve their position and/or image with respect to the previous campaign, to observe at different frequency, or by mistake because a source was not checked thoroughly whether it was observed in previous campaign. The share of unique sources that are detected only in a given campaign is in a range of 0 to 88%.

**Table 1.** The list of 61 VLBI absolute astronomy observing used for deriving the RFC.

Campaign	Network	Id	Reference	Frequency		Dur. Num	Dates		Number of sources			
				low GHz	high GHz		start	end	obs	det	unique	
Pathfinder surveys:												
VCS1	VLBA	bb023	Beasley et al. (2002)	2.3	8.4	264	11	1994.08.12	1997.08.27	1838	1829	1

**Table 1** continued on next page

Table 1 (continued)

Campaign	Network	Id	Reference	Frequency		Dur. Num		Dates		Number of sources		
				low	high		ses	start	end	obs	det	unique
				GHz	GHz	hour						
VCS2	VLBA	bf071	Fomalont et al. (2003)	2.3	8.7	48	2	2002.01.31	2002.05.14	371	366	2
VCS3	VLBA	bp110	Petrov et al. (2005)	2.3	8.7	72	3	2004.04.30	2004.05.27	533	485	0
VCS4	VLBA	bp118	Petrov et al. (2006)	2.3	8.7	72	3	2005.05.12	2005.06.30	504	409	0
VCS5	VLBA	bk124	Kovalev et al. (2007)	2.3	8.7	72	3	2005.07.08	2005.07.20	748	702	0
VCS6	VLBA	bp133	Petrov et al. (2008)	2.3	8.7	48	2	2006.12.18	2007.01.11	347	328	0
VCS7	VLBA	bp171	Petrov (2021)	4.2	7.6	73	17	2013.02.08	2013.08.01	1626	966	490
VCS8	VLBA	bp177	Petrov (2021)	4.4	7.6	48	10	2014.01.07	2014.02.23	1386	926	517
VCS9	VLBA	bp192	Petrov (2021)	4.4	7.6	528	99	2015.08.07	2016.09.07	11016	5673	4234
VCS10-CX	VLBA	bp242	PI: A. Popkov, 2019	4.4	7.6	94	20	2019.07.24	2020.03.17	2778	1488	1232
VCS10-SX	VLBA	bp245u	PI: A. Popkov, 2020	2.3	8.7	23	6	2020.03.02	2020.03.23	638	208	30
VCS11	VLBA	br235	PI: T. Readhead, 2020	4.4	7.6	108	18	2020.09.11	2021.02.16	3326	2616	2292
NPCS	VLBA	bk130	Popkov et al. (2020)	2.3	8.7	72	3	2006.02.14	2006.02.23	526	192	6
V2M	VLBA	bc191	Condon et al. (2017)		8.7	589	94	2010.07.15	2012.06.05	2694	1856	488
VLBApls	VLBA	bh019	Fomalont et al. (2000)	2.3	22.2	16	1	1996.06.05	1996.06.05	228	214	0
	VLBA	bb041	PI: T. Beasley, 1995	2.3	8.4	40	2	1995.06.25	1996.02.16	57	56	0
	VLBA	bm252	Majid et al. (2009)		8.7	20	2	2006.11.06	2006.11.13	74	53	31
VIPS	VLBA	bt085	Helmboldt et al. (2007), Petrov & Taylor (2011)		4.9	174	16	2006.01.03	2006.08.12	858	857	275
	VLBA	bp175	Petrov (2021)	2.3	8.1	43	10	2013.10.26	2013.12.26	405	401	0
	VLBA	s2078	Linford et al. (2012)		4.9	76	7	2009.11.22	2010.07.30	308	308	1
1FGL-VLBI	VLBA	s3111	PI: Y. Kovalev, 2010		8.7	72	3	2010.12.05	2011.01.09	283	279	86
2FGL-VLBIa	VLBA	s4195	PI: Y. Kovalev, 2013		7.6	72	3	2013.05.07	2013.06.22	322	289	142
2FGL-VLBIb	VLBA	bs241	Schinzel et al. (2015)		7.6	54	7	2015.02.16	2015.07.01	451	307	76
2FGL-VLBIc	VLBA	s5272	Schinzel et al. (2015)		7.6	47	4	2013.08.06	2013.12.05	211	153	49
3FGL-VLBI	VLBA	s7104	Schinzel et al. (2017)		7.6	63	9	2016.06.25	2016.07.26	607	416	106
VOFUS-1	VLBA	bs262	PI: F. Schinzel, 2018	4.4	7.6	70	21	2018.04.08	2018.07.24	970	882	335
VOFUS-2	VLBA	sb072	PI: F. Schinzel, 2018	4.4	7.6	110	31	2018.08.25	2019.02.17	1467	1319	575
VGaPS	VLBA	bp125	Petrov et al. (2011a)		24.5	72	3	2006.06.04	2006.10.20	543	533	110
EGaPS	EVN	ep066	Petrov (2012)		22.2	48	1	2009.10.27	2009.10.27	437	186	62
AGaPS	EAVN	ap001a	PI: L. Petrov, 2018		22.2	24	4	2018.10.09	2019.01.28	193	128	0
VEGaPS	VERA	r07030a	PI: L. Petrov, 2007		22.2	28	2	2007.01.30	2007.03.21	125	119	0
GC-KVN	KVN	n20lp01	PI: L. Petrov, 2020	22.7	43.9	69	14	2020.03.05	2020.06.16	400	236	96
OBRS-1	EVN	gc030	Petrov (2011),	2.3	8.4	48	1	2008.03.07	2008.03.07	115	115	1
			Bourda et al. (2011)									
OBRS-2	EVN	gc034	Petrov (2013),	2.3	8.4	216	7	2010.03.23	2012.05.27	378	377	73
			Bourda et al. (2011)									
SOFUS	LBA	sofus	PI: L. Petrov, 2017		8.5	62	3	2017.04.07	2021.02.15	245	149	81
VEPS-1	CVN	veps	Shu et al. (2017)		8.6	425	18	2015.02.13	2017.12.14	4571	878	152
BeSSel-Cal1	VLBA	br145	Immer et al. (2011)		8.4	153	34	2009.11.16	2010.08.29	1536	359	181

Table 1 continued on next page

Table 1 (*continued*)

Campaign	Network	Id	Reference	Frequency		Dur. Num		Dates		Number of sources		
				low	high		ses	start	end	obs	det	unique
				GHz	GHz	hour						
BeSSel-Cal2	VLBA	br149	PI: M. Reid, 2012	2.3	8.0	41	13	2012.08.07	2013.08.04	554	165	59
	VLBA	bg069	Liuzzo et al. (2009)		5.0	44	3	1997.04.06	2005.06.17	60	54	4
	EVN	ec013	Charlot et al. (2004)	8.4	2.3	71	3	2000.05.31	2003.10.17	161	159	0
	VLBA	bu007	Ulvestad et al. (1999)		4.9	12	1	1996.12.19	1996.12.19	163	162	69
	VLBA	bb119	Britzen et al. (2007)		5.0	72	3	1999.11.21	1999.11.26	88	87	0
LCS-1	LBA	v254	Petrov et al. (2011b)		8.4	96	4	2008.02.05	2009.07.04	530	520	167
LCS-2	LBA	v271dr	Petrov et al. (2019)		2.3	368	16	2009.12.12	2016.06.28	1401	948	491
Astrometric follow-up surveys:												
RDV	VLBA	rdv	Petrov et al. (2009)	2.3	8.4	4452	185	1994.07.08	2020.07.07	2045	2012	0
	VLBA	bf025	Fey & Charlot (1997)	2.3	8.4	48	2	1997.01.10	1997.01.11	226	225	0
VEPS-V1	VLBA	bs250	Shu et al. (2017)	2.3	8.7	32	4	2016.03.22	2016.05.19	163	163	0
VEPS-2	VLBA	bs264	PI: F. Shu, 2018	2.3	8.7	48	6	2018.03.21	2018.06.15	357	357	0
VEPS-3	CVN	epa	PI: L. Petrov, 2018	2.3	8.6	44	2	2018.01.24	2018.02.10	182	180	0
GAIA-V1	VLBA	bp222	PI: L. Petrov, 2018	2.3	8.7	304	38	2018.05.15	2020.04.19	1367	1366	0
GAIA-L2	LBA	v561	PI: L. Petrov, 2017	2.3	8.6	71	2	2017.06.16	2018.03.14	306	304	0
VCS-II	VLBA	bg219	Gordon et al. (2016)	2.3	8.7	196	9	2014.01.04	2015.03.17	2597	2588	0
VCS-III	VLBA	uf001	PI: A. Fey, 2017	2.3	8.7	478	20	2017.01.16	2017.10.21	3654	3647	0
VCS-IV	VLBA	ug002	PI: D. Gordon, 2018	2.3	8.7	573	24	2018.01.18	2019.01.21	4416	4235	22
SOAP	LBA	aua	PI: L. Petrov, 2017	2.3	8.6	568	24	2017.08.22	2019.12.04	444	420	6
GC-VLBA	VLBA	bp251	PI: Y. Pihlstrom, 2021	24.0	43.2	8	2	2021.03.19	2021.04.15	53	53	0
	KVN	n13jl01	PI: J. A. Lee, 2013		23.0	196	7	2013.09.04	2014.12.24	790	734	0
High frequency extensions:												
K/Q-Survey	VLBA	br079	Lanyi et al. (2010), Charlot et al. (2010)	24.5	43.2	336	14	2002.05.15	2011.02.05	343	333	0
	VLBA	bj083	PI: A. de Witt, 2015		24.6	105	5	2015.07.21	2016.06.20	286	286	0
	VLBA	ud001	PI: A. de Witt, 2017		23.6	564	24	2017.01.08	2018.07.22	738	738	0
GAJI	KVN	gaji	PI: L. Petrov, 2018	21.7	43.8	22	4	2018.09.25	2018.12.29	151	80	0
Total						12857	909			34003	19687	12542

NOTE—Principal Investigator name is given for the observing campaigns that do not have publications.

Table 1 shows the list of 61 observing campaigns that we used in our work. Most of the observations were made at the Very Long Baseline Array (VLBA) that covers the declination range  $[-40^\circ, +90^\circ]$ . Source at declinations below  $-40^\circ$  were observed with the Long Baseline Array. We used also data, mainly 22 and 43 GHz, from the European VLBI Network (EVN), East Asian VLBI Network (EAVN), Korean VLBI Network (KVN), and VLBI Exploration in Radio Astronomy (VERA). All the data we used on our analysis are in publicly accessible data archives.

### 2.1. Observation Scheduling

A VLBI schedule consists of a table with entries called scans that define for each station start time slewing to a program source, start time for recording baseband data that are digitized voltage from the receiver, and end duration. Upon completion of one scan, the antenna executes another scan. The design of an campaign sets a goal to observe a given source in a number of scans at at least the minimum number of stations at a given integration time per scan. If

the number of scans is greater than one, additional requirements are set, such as the minimum time interval between observation of a given source or observing a source in a minimum time at the specified number of ranges at hour angle of the array reference antenna. Observing at different conditions reduces systematic errors in estimates of source coordinates and improves the *uv*-coverage of program sources which makes imaging more robust. Pathfinder surveys observe target sources in one or two scans. Only a fraction of target sources in such surveys is detected, and even a smaller fraction is detected at at least one half of baselines. Therefore, observing each program source at more scans would increase losses of observing time.

Specialized software prepares the sequence of scans. It consecutively computes the number of antennas that each program source above the physical horizon mask, computes slewing time, computes the likelihood that a given source can be visible at a given minimum number of stations in the future during the observing session and during the campaign, and computes the score that depends on factors mentioned above and other factors. The scan with the highest score is selected for the schedule and the process is repeated. The algorithm for computing the final score is adjusted in such a way that the maximum number of sources is included into the schedule that satisfy the campaign design criteria.

In addition to program sources, a schedule includes observation of known strong sources that are considered as calibrators. A common practice is to include every hour observation of four strong sources selected in such a way that at each station at least one of them is observed at low elevations, for instance  $10^\circ$ – $30^\circ$ , and one source is observed at high elevations, say  $45^\circ$ – $90^\circ$ . The purpose of including of observations of survey calibrators is four-fold: 1) these sources are used as fringe-finders for initialization of the correlation process; 2) these sources are used for computation of the bandpass calibration; 3) these sources are used for improving variable separation for estimation of the residual atmospheric path delay; 4) these sources provide connection of coordinate estimates of program sources with a core of frequently observed sources that define the orientation of the coordinate system. In general 10 to 25% observing time is spent for observing calibrators. Some telescope, like Green Bank Telescope (GBT) and Australia Telescope Compact Array (ATCA) require so-called pointing calibrators that are used for adjusting pointing an high frequency survey may require observations of planets for flux density calibration.

Optimization of the observing schedule that takes into account campaign design goals, placement of calibrators and other constraints. is a very difficult task that is performed by a specialized software (See Petrov 2021; Schartner & Böhm 2020; Schartner et al. 2021, for more details). A campaign consists of segments that are scheduled separately and runs at different days. The scheduling procedure keeps records which sources were observed in prior surveys. For pathfinder surveys that are designed to have one observation per source, a source that is scheduled is removed In order to facilitate optimization the input source list has more source than a campaign can observe. The over-subscription rate is modest, 2–30% for follow-up surveys and large, a factor 1.5 to 4 for pathfinder surveys. The scheduling process selects the freedom to chose in order to maximize the total number of sources. A chance of a given source to be observed can be altered by assigning weight to each source that accounts in calculation of a score. This mechanism is used for fine tuning the selection process: the sources are split into several categories and the weight is assigned according to the category.

For some campaigns observing schedules are prepared in advanced, while most of pathfinder campaigns after 2010 were scheduled dynamically. That means the array operator launches the schedule generation by using a web form when the array has a gap between high priority programs. The principal investigator of observing campaigns scheduled that way loses direct control when and even whether a given source will be observed. At the same time more observing time can be allotted that way.

### 3. DATA ANALYSIS

#### 3.1. *Analysis of visibilities*

#### 3.2. *Analysis of group delays*

### 4. MODELING THE IONOSPHERIC CONTRIBUTION TO PATH DELAY

the impact of the dispersiveness in the ionosphere on fringe phase is reciprocal to frequency in the first approximation. Therefore, fringe phase in channel  $i$  in the presence of the ionosphere becomes

$$\phi_i = 2\pi\tau_p f_0 + \tau_g (f_i - f_0) - \frac{\alpha}{f_i}, \quad (1)$$

where  $\tau_p$  and  $\tau_g$  are phase and group delays,  $f_i$  is the frequency of  $i$ th spectra channel,  $f_0$  is the reference frequency and

$$\alpha = \frac{\pi e^2}{8\pi^2 c m_e \epsilon_o} \left( \int N_v ds_1 - \int N_v ds_2 \right), \quad (2)$$

where  $N_v$  — electron density,  $e$  — charge of an electron,  $m_e$  — mass of an electron,  $\epsilon_o$  — permittivity of free space, and  $c$  — velocity of light in vacuum. Integration is carried along the line of sight. Having substituted values of constants and expressing the total electron contents along the line of sight  $\int N_v ds$  in  $1 \cdot 10^{16}$  electrons/ $m^2$  (so-called TEC units or TECU), we arrive to  $\alpha = 1.344537 \cdot 10^{10} \text{ sec}^{-1}$ .

Phase and group delay are computed using fringe phases  $\phi_i$  with weights  $w_i$  using least squares. The result can be expressed analytically after some algebra:

$$\tau_{gi} = \tau_{if} + \frac{\alpha}{f_e^2} \text{TEC}, \quad (3)$$

where  $\tau_{if}$  is the ionosphere-free group delay, TEC is  $\int N_v ds$  expressed in TEC units and  $f_e$  is the effective ionosphere frequency

$$f_e = \sqrt{\frac{\sum_i^n w_i \cdot \sum_i^n w_i (f_i - f_0)^2 - \left( \sum_i^n w_i (f_i - f_0) \right)^2}{\sum_i^n w_i (f_i - f_0) \sum_i^n \frac{w_i}{f_i} - \sum_i^n w_i \cdot \sum_i^n w_i \frac{(f_i - f_0)}{f_i}}}. \quad (4)$$

The best way to mitigate the impact of the ionosphere on group delay is to observe simultaneously at two or more widely separated frequency bands. Then the following linear combination of two group delays at the upper and lower bands,  $\tau_u$  and  $\tau_l$ , respectively is ionosphere free:

$$\tau_{if} = \frac{f_u^2}{f_u^2 - f_l^2} \tau_u - \frac{f_l^2}{f_u^2 - f_l^2} \tau_l. \quad (5)$$

Here  $f_u$  and  $f_l$  are effective ionospheric frequencies at the upper and lower bands respectively.

The residual contribution of the ionosphere is caused by a) higher order terms in the expansion of the dispersiveness on frequency (Hawarey et al. 2005); b) the contribution of frequency-dependent source structure, and c) the dispersiveness in the signal chain. These contributions affect group delay at a level of several ps and considered insignificant with respect to other systematic errors.

For processing single band observations TEC maps derived from analysis of Global Navigation Satellite System (GNSS) are used. In particular, we used CODE TEC time series (Schaer 1999)<sup>1</sup> available since January 01 1995 with a spatial resolution of  $5^\circ \times 2.5^\circ$ . Time resolution was  $24^h$  since 01 January 1995 through February 01, 1995 through March 27, 1998,  $2^h$  since March 28, 1998 through October 18, 2014 and  $1^h$  after that date. The ionosphere is considered as a thin shell at the height  $H_i$  of 450 km above the surface. The ionospheric contribution is

$$\tau_i = \frac{\alpha}{f_e^2} \text{TEC} \frac{1}{\cos \beta}, \quad (6)$$

where  $\beta$  is the zenith angle at the ionosphere piercing point that depends on the elevation angle  $E$  as

$$\beta = \arcsin \frac{\cos E}{1 + \frac{H_i}{R_\oplus}}, \quad (7)$$

where  $R_\oplus$  is the Earth radius.

<sup>1</sup> Available at <ftp://ftp.aiub.unibe.ch/CODE>

The TEC maps from GNSS is a coarse model of the ionosphere. Errors of  $\tau_i$  computed according to expression 6 are much greater than the residual ionosphere contribution of ionosphere-free linear combinations of group delays. We always use dual-band delay observables when they are available. However, there are two cases when they are not available: a) dual band observing sessions with some source detected only at one band; b) single band observing sessions. In these two cases we compute ionospheric contribution to path delays using GNSS TEC maps and evaluate uncertainties of these contributions.

#### 4.1. Ionospheric contribution in dual-band observing sessions when a source is detected at one band only

The simplest way is to process an experiment three times: using dual-band data of those observations that detected a source in both band, using a low band and an upper band with applying ionospheric path delay using TEC maps from GNSS. However, typically only a fraction, 2 to 20% of observations is detected at only one band; the rest of observations are detected at both bands. Therefore, we can use available dual-band observations at a given observing session to improve the TEC model.

We represent ionospheric path delay at stations  $j, k$  as

$$\tau_i(t) = b_j(t) - b_k(t) + \frac{\alpha}{f_e^2} \left( \left( \text{TEC}_j(\phi_j, \lambda_j, t) + a_j(t) \right) M(e_j) - \left( \text{TEC}_k(\phi_k, \lambda_k, t) + a_k(t) \right) M(e_k) \right), \quad (8)$$

where  $b_j(t) = \sum_i^n B_i^0(t) b_{ij}$  is a delay bias expanded over the B-spline basis of the 0th degree,  $a_j(t) = \sum_i^n B_i^3(t) a_{ij}$  is the TEC bias expanded over the B-spline basis of the 3rd degree, and  $M(e) = 1/\cos \beta$  is the ionosphere mapping function.  $\phi, \lambda$  are coordinates of the ionosphere piercing point that depend on positions of observing station, and azimuths and elevations.

The clock bias occurs due to path delay in the VLBI hardware that is different at different bands. This bias is constant for most of the experiments, however occasionally breaks may happen at some stations. Epochs of these breaks coincide with the epochs of breaks in clock function. Expansion over the B-spline basis of the 0th degree accounts for these breaks. (B-spline of the 0th degree is 1 within the range of knots  $[i, i+1]$  and 0 otherwise.)

We estimated parameters  $a_j$  for all the stations and  $b_j$  for all the stations except the one taken as a reference using all available dual-band observations of a given experiment using least squares with weights

$$w_i = \frac{1}{\sqrt{y^2 + \frac{f_u^4 \sigma^2(\tau_u) + f_l^4 \sigma^2(\tau_l)}{(f_u^2 - f_l)^2}}}. \quad (9)$$

where  $y$  is the error floor, 12 ps, introduced to avoid observations with very high SNR to dominate the solution.

The time span of the B-spline knot sequence for TEC bias in our solutions was 15 minutes. We applied constraints on the value of the B-spline coefficients, the first, and the second derivative with reciprocal weights  $5 \cdot 10^{-10} \text{ s}$ ,  $4 \cdot 10^{-14}$ , and  $2 \cdot 10^{-18} \text{ s}^{-1}$  respectively. This constraints were applied to ensure the continuity of biases and to prevent a singularity in rare cases when too few available observations at a given station could be used for bias estimation at a given spline segment. Figure 1 illustrates estimates of the ionospheric bias.

The resulting total electron contents model  $\text{TEC}_j(t) + a_j(t)$  is more precise than the a priori  $\text{TEC}_j(t)$  taken from GNSS maps because it uses additional information. Using estimates of  $a_j$  and  $b_j$  spline coefficients, we compute  $\tau_i(t)$  and its uncertainty according to the law of error propagation using the full variance-covariance matrix of the spline estimate coefficients. In order to evaluate the realism of these errors, we have processed 262 twenty-four hour VLBA observations since April 1998 though March 2021 and computed  $\tau_i(t)$  using the estimates of clock and TEC biases and compared them with the ionospheric contribution derived from the dual-band observations. We removed clock biases from VLBI dual band ionospheric contributions  $\tau_{vi}$ , formed the differences  $\tau_i - \tau_{vi}$  and divided then by  $\sigma(\tau_i)$  derived from the variance-covariance matrix of  $a_j, b_j$ . We generated the normalized histogram from the dataset of 4,343,782 differences and computed two moments of the empirical distribution shown in Figure 2). The fitting parameters of the first and second moments of the distribution are 0.003 and 0.889 respectively. Two factors cause a deviation of the second moment from 1.0 in the opposite sides: a) TEC variations not accounted by the parametric model; b) statistical dependence of the estimates of  $a_j, b_j$  and VLBI path delay used in least squares. After scaling the variance-covariance matrix by  $0.889^2$ , the distribution of the normalized residuals becomes close to Gaussian. The closeness of the empirical distribution to the normal distribution provides us a confidence that extra noise introduced by the mismodeled ionospheric path delay after applying clock and TEC biases is properly accounted.

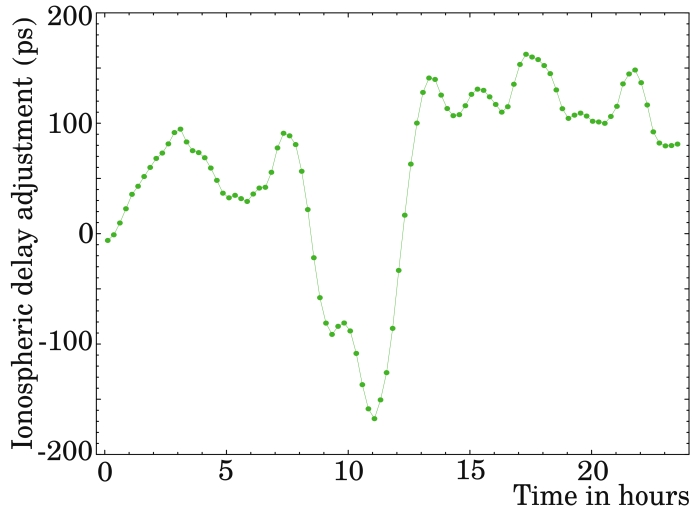


**Figure 1.** Adjustment to the ionosphere path delay bias at 8.4 GHz with respect to the path delay derived from GNSS TEC maps at MK-VLBA station from processing of dual-band observations on April 22, 2015.

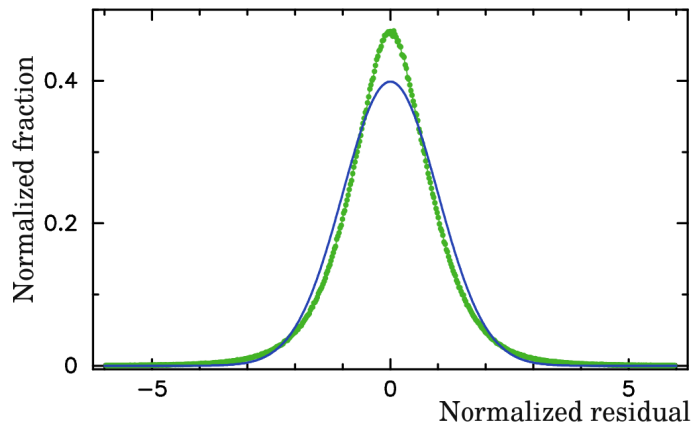


**Figure 2.** Empirical distribution of the normalized differences of the ionosphere path delay computed from the GNSS TEC maps adjusted for clock and TEC biases (green dots). The normal distribution with  $\sigma = 1$  is shown as a reference (solid blue line).

#### 4.2. Ionospheric contribution in single-band observing sessions

When an entire session is observed only at one band, TEC biases cannot be computed. Therefore, we have to resort to deriving a regression model to provide estimates of these errors. In the past, Petrov et al. (2019) derived a regression against the so-called global TEC: the integral of TEC over the entire Earth following ideas of Afraimovich et al. (2008) and Krásná & Petrov (2021) derived a regression against the rms of the total path delay from GNSS TEC. In this study we use the second approach with slight modifications. Following general results of the turbulence theory (see Tatarskii 1971), we can expect that fluctuations at scales  $x$  are related to fluctuations at scales  $y$  via a power law.

We processed the same dataset of 262 twenty-four hour VLBI experiments that we used in the previous subsection and computed residual ionospheric path delay for each observation as

$$\tau_r = (\tau_{\text{gi}} - \tau_{\text{vi}} - c_i) \tilde{M}, \quad (10)$$

where  $\tau_{\text{gi}}$  is the ionospheric path delay from GNSS TEC maps,  $\tau_{\text{vi}}$  is the ionospheric path delay from VLBI,  $c_i$  contribution of the clock bias, and  $\tilde{M}$  is the averaged ionosphere mapping function between stations 1 and 2 of a given baseline:  $\tilde{M} = (M(e_1) + M(e_2))/2.0$ . The clock biases are routinely adjusted during analysis of VLBI observations and therefore, their contribution on VLBI results, such as source positions is entirely eliminated. Subtracting them in expression 10, we eliminate their impact on statistics as well. We used only twenty-four hour VLBI experiments for

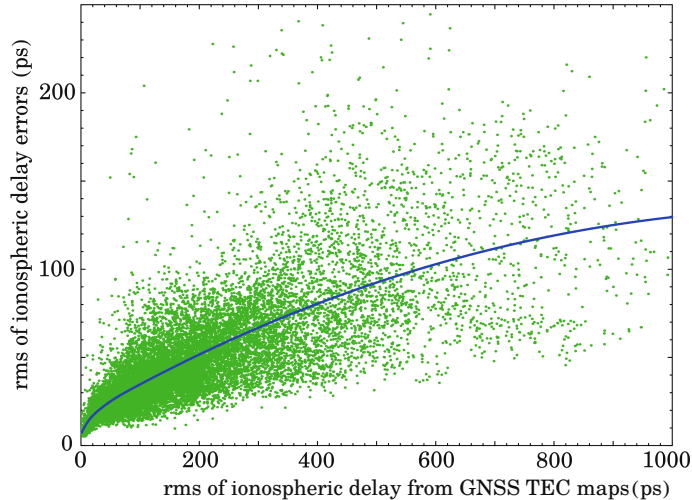


**Figure 3.** Dependence of the rms of residual ionospheric path delay derived from GNSS TEC maps on the rms of the total ionospheric path delay from these maps. No adjustment to TEC has been applied. Path delay is computed for the reference frequency 8 GHz. The blue smooth line shows the regression model in a form of a B-spline that fits the data.

**Table 2.** Coefficients of the B-spline expansion of Dependence of the rms of residual ionospheric path delay derived from GNSS TEC maps on the rms of the total ionospheric path delay from GNSS maps at 8 GHz.

knot index	knot argument (ps)	B-spline value (ps)
-2		5.08507
-1		12.52318
0		24.64614
1	0.0	114.00000
2	20.0	114.00000
3	120.0	114.00000
4	1300.0	

deriving statistics because the ionospheric path delay strongly depends on Solar time, especially at low latitudes, and statistics derived at shorter time intervals are not representative.

Figure 3 shows the dependence of rms of residuals  $\tau_r$  on the total ionospheric path delay from GNSS TEC maps  $\tau_{gi}$ . Each point on the plot corresponds to the rms for a given baseline and given observing session. We confirm an early result of Krásná & Petrov (2021) but here we used a much larger dataset. Result of Krásná & Petrov (2021) was affected by an error in computation of group delays for a case when some data are flagged because of radio interference. This error was fixed and affected dataset was reprocessed from scratches. This dependence can be coarsely described as a square root of the total ionospheric path delay. For a better approximation, we sought the regression in the form of expansion of basis spline of the 3rd degree. The spline coefficients computed using least squares are listed in Table 2.

This regression suggests the following algorithm for computation of errors of the ionospheric path delay from GNSS TEC. Using a random number generator we compute  $K$  points uniformly distributed over the sphere. Then for each baseline and each time epoch we compute the azimuth and elevation angle of that point at both stations of the baseline, and if the elevation above are greater than  $5^\circ$ , that point is selected for further computations. If not, the next point is drawn. Then we compute quantity  $\tau_r(A_1, e_1, A_2, e_2)$  from expression 10. It is worth mentioning here that unlike to tropospheric path delay,  $\tau_i(A, e) \neq \tau_i(A, \pi/2) M(e)$ , since path delay depends on positions of the ionosphere piercing point. It is not sufficient to compute the ionospheric path delay in zenith direction and then map it via  $M(e)$ : latitude and longitude of the piercing point can be as far as 1000 km from the station. In our approach we sample piercing

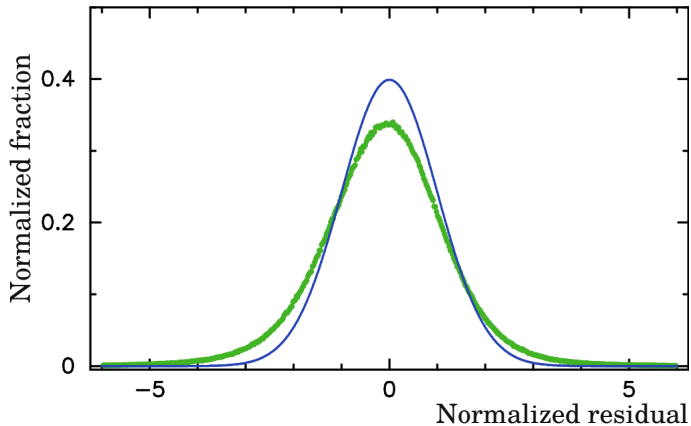


**Figure 4.** The distribution of the normalized differences of the ionosphere path delay computed from the GNSS TEC maps against VLBI ionospheric path delay with clock biases subtracted (green dots). The normal distribution with  $\sigma = 1$  (solid blue line) is shown as a reference.

points uniformly distributed within a the mutual visibility zone. The process is repeated for 1440 time epochs with a step of 1 minute. Then for each baseline we compute  $\sigma(\tau_r)$ . Finally, the error estimate of the ionospheric path delay derived from the GNSS TEC maps is computed from the regression:

$$\sigma_{\text{gi}} = \sigma(\tau_r) \sum_k^n B_k^3(\tau_r) \sqrt{M^2(e_1) + M^2(e_2)}. \quad (11)$$

Baseline are considered independent for this simulation: the mutual visibility at all the stations of the network at a given moment of time is not enforced. For several baselines longer than 96% Earth diameter, this algorithms has a poor performance for selecting a point above  $5^\circ$ . Therefore a minor modification is made for that case: the elevation angle is fixed to  $5^\circ$ , we do not enforce mutual visibility and select azimuths randomly within a range of  $[0, 2\pi]$ , independently for both stations.

In order to evaluate the validity of this regression model for ionospheric path delay model, we computed  $\tau_r$  and  $\sigma_{\text{gi}}$  for 262 twenty-four experiments and computed the histograms of normalized residuals  $\tau_r/\sigma_{\text{gi}}$ . The histogram is presented in Figure 4. The first two moments of the distribution are -0.083 and 1.214 respectively. Since the regression for  $\sigma(\tau_r)$  was found using least square, the number of observations with  $\sigma(\tau_r)$  less and greater than  $\sigma_{\text{gi}}$  for given  $\tau_r$  is approximately equal. However, the variance of the contribution of points with  $\tau_r$  that are greater than the mean overweighs the contribution of points with  $\tau_r$  that are less than the mean because covariance non-linear depends on  $\tau_r$ . This contributes to a positive bias. After multiplying  $\sigma_{\text{gi}}$  by 1.214, the distribution of normalized residuals becomes almost Gaussian.

One can notice that  $\sqrt{M^2(e_1) + M^2(e_2)}$  in expression 11 is not the same as  $\tilde{M} = (M(e_1) + M(e_2))/2$  used for computation of the regression. We found that using  $\tilde{M}$  instead of  $\sqrt{M^2(e_1) + M^2(e_2)}$  decreases the second moment from to 1.214 to 1.196, which is negligible,

The distributions shown in Figures 2 and 4 are computed for the entire dataset of 4.3 million path delays and their represent the population in general for the interval of 23 years. Statistics for an individual observing session may differ. In order to evaluate the scatter of the statistics, we computed the time series of second moments of the distribution of normalized residuals of ionospheric path delays and their uncertainties with and without TEC biases adjusted for each observing session separately. We divided the normalized residuals by scaling factors of 0.889 and 1.196 respectively. We computed the distribution of the second moment estimates and showed them in Figure 5. The scatter of the second moments is small when TEC biases are adjusted. That means the statistics are robust. When the TEC is not adjusted, the scatter is significantly larger, but even in that case 90% of the second moment estimates deviate from 1.0 by no more than 30%. This provides us a measure of uncertainties of computation of ionospheric path delay errors for single-band observing sessions.

Finally, we computed the rms of the residual ionospheric contributions for 45 VLBA baselines for the dateset of 262 twenty-four observing sessions. We computed three statistics for each observing session: 1)  $\tau_v - b_i$ , 2)  $\tau_v - \tau_g - b_i$ ; and 3)  $\tau_v - \tau_g - a_i - b_i$ ,  $\tau_v$ . Here  $\tau_g$  is the ionospheric path delay from VLBI and TEC maps,  $a_i$  is the adjusted TEC

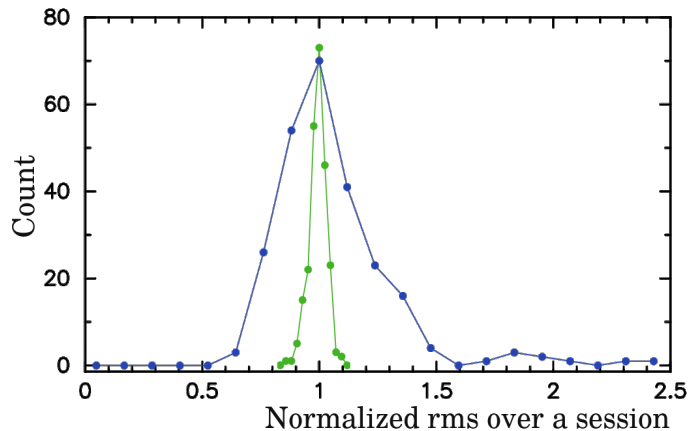


**Figure 5.** The distribution of second moment estimates of the normalized differences of ionospheric path delays derived from VLBI dual-band observations and GNSS TEC maps among individual observing sessions. The narrow green curve shows the statistics of the normalized residuals with TEC biases adjusted and the wide blue curve show the statistics of normalized residuals without TEC adjustment.

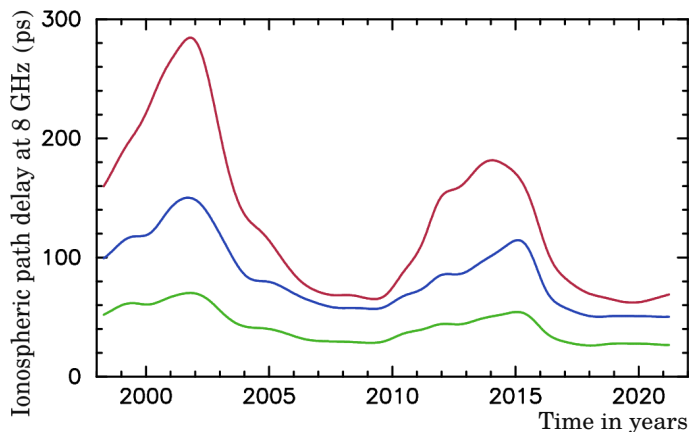


**Figure 6.** rms of the the mean residual ionospheric contribution at VLBA baseline at 8 GHz for three cases: 1) no ionospheric contribution is applied (upper red curve); 2) ionospheric path delay computed using GNSS TEC maps is applied (middle blue curve); and 3) ionospheric path delay computed using GNSS TEC maps are applied and TEC biases are adjusted (lower green curve).

bias, and  $b_i$  is clock biases. The statistics are shown in Figure 6. In order to improve readability, the time series were smoothed using Gaussian kernel with parameter  $\sigma = 1$  year.

#### 4.3. Computation of path delay for data analysis

We have computed clock and TEC biases for all dual-band observing sessions. In a case if group delays at both bands are usable in the analysis, we used the ionosphere-free combinations of dual-band group delays according to expression 6. If group delay at one of the band was not useful, f.e. the source was not detected, but the second band had a usable group delay we computed ionospheric path delay using expression 8 and the uncertainty of that contribution multiplied by an empirical fudge factor 0.889. That uncertainty was added in quadrature to the group delay uncertainty.

When we process single-band observing sessions for each baseline we computed the rms of the total GNSS path delay over a 24 hour period center around the middle epoch of observations using the procedure described in the previous subsection. This quantity scaled by the mean ionospheric mapping function  $\sigma_{gi} \bar{M}$  is added in quadrature to the uncertainty of a single-band group delay.

NVSS	$-40^\circ < 90^\circ$	18036	100%
SUMSS	$-90^\circ < -30^\circ$	2616	95%
ALL-WISE	$-90^\circ < 90^\circ$	15098	77%
TGSS	$-53^\circ < 90^\circ$	13688	73%
PanSTARRS	$-30^\circ < 90^\circ$	11618	69%
Gaia EDR3	$-90^\circ < 90^\circ$	12009	62%
AT20G	$-90^\circ < 0^\circ$	4317	51%
GALEX	$-90^\circ < 90^\circ$	6233	32%
ROSAT	$-90^\circ < 90^\circ$	3625	19%
2RXS	$-90^\circ < 90^\circ$	2936	15%
2CXPS	$-90^\circ < 90^\circ$	2958	15%
FERMI	$-90^\circ < 90^\circ$	2809	14%
2CXO	$-90^\circ < 90^\circ$	2708	14%
BZCAT	$-90^\circ < 90^\circ$	2382	12%
2MASS	$-90^\circ < 90^\circ$	1728	9%

Since we have a reliable estimate of errors of residual ionospheric contribution, we can fuse single-band and dual-band data and process both data in a single least square solution. This is a novel approach and it allows to get the best astrometric solution for a case when some data point have only one point.

#### 4.4. *Global parameter estimation*

### 5. ERROR ANALYSIS

#### 5.1. *Errors of dual-band observations*

#### 5.2. *Errors of single-band observations*

#### 5.3. *Reweighting*

### 6. MULTIPLE SOURCES

### 7. THE CATALOGUE

### 8. SUMMARY

## REFERENCES

- Afraimovich, E. L., Astafyeva, E. I., Oinats, A. V., Yasukevich, Y. V., & Zhivetiev, I. V. 2008, *Annales Geophysicae*, 26, 335, doi: [10.5194/angeo-26-335-2008](https://doi.org/10.5194/angeo-26-335-2008)
- Ajello, M., Angioni, R., Axelsson, M., et al. 2020, *The Astrophysical Journal*, 892, 105, doi: [10.3847/1538-4357/ab791e](https://doi.org/10.3847/1538-4357/ab791e)
- Beasley, A. J., Gordon, D., Peck, A. B., et al. 2002, *ApJS*, 141, 13, doi: [10.1086/339806](https://doi.org/10.1086/339806)
- Bourda, G., Collioud, A., Charlot, P., Porcas, R., & Garrington, S. 2011, *A&A*, 526, A102, doi: [10.1051/0004-6361/201014249](https://doi.org/10.1051/0004-6361/201014249)
- Britzen, S., Vermeulen, R. C., Taylor, G. B., et al. 2007, *A&A*, 472, 763, doi: [10.1051/0004-6361:20052677](https://doi.org/10.1051/0004-6361:20052677)
- Charlot, P., Fey, A. L., Jacobs, C. S., et al. 2004, in *European VLBI Network on New Developments in VLBI Science and Technology*, 313–316
- Charlot, P., Boboltz, D. A., Fey, A. L., et al. 2010, *AJ*, 139, 1713, doi: [10.1088/0004-6256/139/5/1713](https://doi.org/10.1088/0004-6256/139/5/1713)
- Cohen, M. H., & Shaffer, D. B. 1971, *AJ*, 76, 91, doi: [10.1086/111090](https://doi.org/10.1086/111090)
- Condon, J. J., Darling, J., Kovalev, Y. Y., & Petrov, L. 2017, *ApJ*, 834, 184, doi: [10.3847/1538-4357/834/2/184](https://doi.org/10.3847/1538-4357/834/2/184)
- Fanselow, J. L., Sovers, O. J., Thomas, J. B., et al. 1984, *AJ*, 89, 987, doi: [10.1086/113594](https://doi.org/10.1086/113594)
- Fey, A. L., & Charlot, P. 1997, *ApJS*, 111, 95, doi: [10.1086/313017](https://doi.org/10.1086/313017)
- Fomalont, E. B., Frey, S., Paragi, Z., et al. 2000, *ApJS*, 131, 95, doi: [10.1086/317368](https://doi.org/10.1086/317368)
- Fomalont, E. B., Petrov, L., MacMillan, D. S., Gordon, D., & Ma, C. 2003, *AJ*, 126, 2562, doi: [10.1086/378712](https://doi.org/10.1086/378712)
- Gordon, D., Jacobs, C., Beasley, A., et al. 2016, *AJ*, 151, 154, doi: [10.3847/0004-6256/151/6/154](https://doi.org/10.3847/0004-6256/151/6/154)

- Hawarey, M., Hobiger, T., & Schuh, H. 2005, *Geophys. Res. Lett.*, 32, L11304, doi: [10.1029/2005GL022729](https://doi.org/10.1029/2005GL022729)
- Helmboldt, J. F., Taylor, G. B., Tremblay, S., et al. 2007, *ApJ*, 658, 203, doi: [10.1086/511005](https://doi.org/10.1086/511005)
- Immer, K., Brunthaler, A., Reid, M. J., et al. 2011, *ApJS*, 194, 25, doi: [10.1088/0067-0049/194/2/25](https://doi.org/10.1088/0067-0049/194/2/25)
- Jones, D. L., Folkner, W. M., Jacobson, R. A., et al. 2020, *AJ*, 159, 72, doi: [10.3847/1538-3881/ab5f5d](https://doi.org/10.3847/1538-3881/ab5f5d)
- Kovalev, Y. Y., Petrov, L., Fomalont, E. B., & Gordon, D. 2007, *AJ*, 133, 1236, doi: [10.1086/511157](https://doi.org/10.1086/511157)
- Krásná, H., & Petrov, L. 2021, *Journal of Geodesy*, 95, 101, doi: [10.1007/s00190-021-01551-3](https://doi.org/10.1007/s00190-021-01551-3)
- Lanyi, G. E., Boboltz, D. A., Charlot, P., et al. 2010, *AJ*, 139, 1695, doi: [10.1088/0004-6256/139/5/1695](https://doi.org/10.1088/0004-6256/139/5/1695)
- Linford, J. D., Taylor, G. B., Romani, R. W., et al. 2012, *ApJ*, 744, 177, doi: [10.1088/0004-637X/744/2/177](https://doi.org/10.1088/0004-637X/744/2/177)
- Liuzzo, E., Giovannini, G., Giroletti, M., & Taylor, G. B. 2009, *A&A*, 505, 509, doi: [10.1051/0004-6361/200912586](https://doi.org/10.1051/0004-6361/200912586)
- Ma, C., Arias, E. F., Eubanks, T. M., et al. 1998, *AJ*, 116, 516, doi: [10.1086/300408](https://doi.org/10.1086/300408)
- Majid, W. A., Fomalont, E. B., & Bagri, D. S. 2009, in *Astronomical Society of the Pacific Conference Series*, Vol. 402, *Approaching Micro-Arcsecond Resolution with VSOP-2: Astrophysics and Technologies*, ed. Y. Hagiwara, E. Fomalont, M. Tsuboi, & M. Yasuhiro, 448
- Martí-Vidal, I., Ros, E., Pérez-Torres, M. A., et al. 2010, *A&A*, 515, A53, doi: [10.1051/0004-6361/201014203](https://doi.org/10.1051/0004-6361/201014203)
- Matveenko, L. I., Kardashev, N.-S., & Sholomitskii, G.-B. 1965, *Soviet Radiophys.*, 461, 461
- Morabito, D. D., Niell, A. E., Preston, R. A., et al. 1986, *AJ*, 91, 1038, doi: [10.1086/114080](https://doi.org/10.1086/114080)
- Petrov, L. 2011, *AJ*, 142, 105, doi: [10.1088/0004-6256/142/4/105](https://doi.org/10.1088/0004-6256/142/4/105)
- . 2012, *MNRAS*, 419, 1097, doi: [10.1111/j.1365-2966.2011.19765.x](https://doi.org/10.1111/j.1365-2966.2011.19765.x)
- . 2013, *AJ*, 146, 5, doi: [10.1088/0004-6256/146/1/5](https://doi.org/10.1088/0004-6256/146/1/5)
- . 2021, *AJ*, 161, 14, doi: [10.3847/1538-3881/abc4e1](https://doi.org/10.3847/1538-3881/abc4e1)
- Petrov, L., de Witt, A., Sadler, E. M., Phillips, C., & Horiuchi, S. 2019, *MNRAS*, 485, 88, doi: [10.1093/mnras/stz242](https://doi.org/10.1093/mnras/stz242)
- Petrov, L., Gordon, D., Gipson, J., et al. 2009, *Journal of Geodesy*, 83, 859, doi: [10.1007/s00190-009-0304-7](https://doi.org/10.1007/s00190-009-0304-7)
- Petrov, L., Kovalev, Y. Y., Fomalont, E. B., & Gordon, D. 2005, *AJ*, 129, 1163, doi: [10.1086/426920](https://doi.org/10.1086/426920)
- . 2006, *AJ*, 131, 1872, doi: [10.1086/499947](https://doi.org/10.1086/499947)
- . 2008, *AJ*, 136, 580, doi: [10.1088/0004-6256/136/2/580](https://doi.org/10.1088/0004-6256/136/2/580)
- . 2011a, *AJ*, 142, 35, doi: [10.1088/0004-6256/142/2/35](https://doi.org/10.1088/0004-6256/142/2/35)
- Petrov, L., Mahony, E. K., Edwards, P. G., et al. 2013, *MNRAS*, 432, 1294, doi: [10.1093/mnras/stt550](https://doi.org/10.1093/mnras/stt550)
- Petrov, L., Phillips, C., Bertarini, A., Murphy, T., & Sadler, E. M. 2011b, *MNRAS*, 414, 2528, doi: [10.1111/j.1365-2966.2011.18570.x](https://doi.org/10.1111/j.1365-2966.2011.18570.x)
- Petrov, L., & Taylor, G. B. 2011, *AJ*, 142, 89, doi: [10.1088/0004-6256/142/3/89](https://doi.org/10.1088/0004-6256/142/3/89)
- Popkov, A. V., Kovalev, Y. Y., Petrov, L. Y., & Kovalev, Y. A. 2020, arXiv e-prints, arXiv:2008.06803. <https://arxiv.org/abs/2008.06803>
- Preston, R. A., Morabito, D. D., Williams, J. G., et al. 1985, *AJ*, 90, 1599, doi: [10.1086/113869](https://doi.org/10.1086/113869)
- Reid, M. J., & Honma, M. 2014, *ARA&A*, 52, 339, doi: [10.1146/annurev-astro-081913-040006](https://doi.org/10.1146/annurev-astro-081913-040006)
- Reid, M. J., Brunthaler, A., Menten, K. M., et al. 2017, *AJ*, 154, 63, doi: [10.3847/1538-3881/aa7850](https://doi.org/10.3847/1538-3881/aa7850)
- Schaer, S. 1999, *Geod.-Geophys. Arb. Schweiz*, Vol. 59., 59
- Schartner, M., & Böhm, J. 2020, *Journal of Geodesy*, 94, 12, doi: [10.1007/s00190-019-01340-z](https://doi.org/10.1007/s00190-019-01340-z)
- Schartner, M., Plötz, C., & Soja, B. 2021, *Journal of Geodesy*, 95, 58, doi: [10.1007/s00190-021-01512-w](https://doi.org/10.1007/s00190-021-01512-w)
- Schinkel, F. K., Petrov, L., Taylor, G. B., & Edwards, P. G. 2017, *ApJ*, 838, 139, doi: [10.3847/1538-4357/aa6439](https://doi.org/10.3847/1538-4357/aa6439)
- Schinkel, F. K., Petrov, L., Taylor, G. B., et al. 2015, *ApJS*, 217, 4, doi: [10.1088/0067-0049/217/1/4](https://doi.org/10.1088/0067-0049/217/1/4)
- Shu, F., Petrov, L., Jiang, W., et al. 2017, *ApJS*, 230, 13, doi: [10.3847/1538-4365/aa71a3](https://doi.org/10.3847/1538-4365/aa71a3)
- Tatarskii, V. I. 1971, *The effects of the turbulent atmosphere on wave propagation*
- Ulvestad, J. S., Fomalont, E. B., & Kimora, H. 1999, in *American Astronomical Society Meeting Abstracts*, Vol. 194, *American Astronomical Society Meeting Abstracts #194*, 50.23

## APPENDIX

**Potom razberyom, kuda eto delo zasunut'****Corr 3**

## Pathfinder surveys:

1. VLBA Calibrator survey 1 (VCS1), (Beasley et al. 2002); VLBA BB023; S/X bands; 11 segments; since 1994.08.12 through 1997.08.27.
2. VLBA Calibrator survey 2 (VCS2), (Fomalont et al. 2003); VLBA BB071; S/X bands; 2 segments; since 2002.01.31 through 2002.05.14.
3. VLBA Calibrator survey 3 (VCS3), (Petrov et al. 2005); VLBA BP110; S/X bands; 3 segments; since 2004.04.30 through 2004.05.27.
4. VLBA Calibrator survey 4 (VCS4), (Petrov et al. 2006), VLBA BP118; S/X bands; 3 segments; since 2005.05.12 through 2005.06.30.
5. VLBA Calibrator survey 5 (VCS5), (Petrov et al. 2006), VLBA BK124; S/X bands; 3 segments; since 2005.07.08 through 2005.07.20.
6. VLBA Calibrator survey 6 (VCS6), (Petrov et al. 2008), VLBA BP133; S/X bands; 3 segments; since 2006.12.18 through 2007.01.11.
7. VLBA Calibrator Densification 7 (VCS7), (Petrov 2021); VLBA BP171; C/X bands; 17 segments; since 2013.02.08 through 2013.08.01.
8. VLBA Calibrator Densification 8 (VCS8), (Petrov 2021); VLBA BP177; C/X bands; 10 segments; since 2014.01.07 through 2014.02.23.
9. VLBA Calibrator Densification 9 (VCS9), (Petrov 2021); VLBA BP192; C/X bands; 99 segments; since 2015.08.07 through 2016.09.07.
10. Study of the population of steep-spectrum compact radio sources, 1st part (VCS10); VLBA BP242; C/X bands; 19 segments; since 2019.07.24 through 2020.02.11.
11. Study of the population of steep-spectrum compact radio sources, 2nd part (VCS10); VLBA BP245; S/X bands; 6 segments; since 2020.03.02 through 2020.03.23.
12. Completion of Surveys for a Gravitational Lens Search to Explore Dark Matter (VCS11), PI: T. Readhead; VLBA BR235; 18 segments; since 2020.09.11 through 2021.02.16.
13. Northern Polar Cup Survey, Popkov et al. (2020); VLBA BK130; X band; 3 segments; since 2006.02.14 through 2006.02.23
14. A systematic search for inspiraling, binary, and recoiling black holes in nearby galaxies (V2M), Condon et al. (2017); VLBA BC191, BC196, BC201; X band; 94 segments; since 2010.07.15 through 2012.06.05.
15. The VSOP Pre-launch VLBA Observations (VLBApls), (Fomalont et al. 2000); VLBA BH019; C band; 1 segment; 1996.06.05.
16. BB041, PI: T. Beasley; VLBA BB041; S/X bands; 2 segments; since 1995.06.25 through 1995.02.16.
17. Compactness of Weak Radio Sources at High Frequencies, (Majid et al. 2009); VLBA BM252; X-band; 2 segments; since 2006.11.06 through 2006.11.13.
18. VLBA Imaging and Polarimetry Survey at 5 GHz, (VIPS), (Helmholtz et al. 2007; Petrov & Taylor 2011); VLBA BT085; C-band; 16 segments; since 2006.01.03 through 2006.08.12.

19. Low Luminosity gamma-ray blazars (Linford et al. 2012); VLBA S2078, BT110; C-band; 7 segments; since 2009.11.22 through 2010.07.30.
20. 1FGL Active Galactic Nuclei at parsec scales, PI: Y. Kovalev; VLBA S3111; X-band; 3 segments; since 2010.12.05 through 2011.01.09.
21. 2FGL Active Galactic Nuclei at Parsec Scales, PI: Y. Kovalev; VLBA S4195; X-band; 3 segments; since 2013.05.07 through 2013.06.22.
22. 2FGL AGNs at parsec scales, 2nd survey, (Schinzel et al. 2015); VLBA BS241; X-band; 7 segments; since 2015.02.16 through 2015.07.01.
23. VLBI follow-up of Fermi sources, (Schinzel et al. 2015); VLBA S5272; X-band, 4 segments; since 2013.08.06 through 2013.12.05.
24. 3FGL at parsec scales, (Schinzel et al. 2017); VLBA S7104; X-band; 9 segments; since 2016.06.27 through 2016.07.26.
25. VLBA Survey of unassociated gamma-ray objects in the 7-year Fermi/LAT catalog, PI: F. Schinzel, VLBA BS262; C/X bands; 21 segments; since 2018.04.08 through 2018.07.24.
26. VLBA Survey of unassociated gamma-ray objects in the 7-year Fermi/LAT catalog, 2nd survey; PI: F. Schinzel; VLBA SB072; C/X bands; 31 segments; since 2018.08.25 through 2019.02.17.
27. The VLBA Galactic Plane Survey (VGaPS), (Petrov et al. 2011a); VLBA BP125; K band; 3 segments; since 2006.02.04 through 2006.10.20.
28. The EVN Galactic Plane Survey (EGaPS), (Petrov 2012); EVN EP066; K band; 1 segment; 2009.10.27.
29. Detection of the background position noise due to non-stationary of the Galactic gravitational field, PI: L. Petrov, KVN GAJI; K/Q bands; 5 segments; since 2018.09.25 through 2018.12.29.
30. VERA Galactic Plane Survey, PI: L. Petrov; VERA R07030A, R07100A; K band; 2 segments; since 2007.01.30 through 2007.03.21.
31. Asian VLBI Galactic Plane Survey, PI: L. Petrov; EAVN AP001A; K band; 4 segments; since 2018.10.09 through 2019.01.28.
32. A search for high-frequency calibrators within 10 degrees of the Galactic center, PI: L. Petrov; KVN N20LP01; K/Q bands; 14 segments; since 2020.03.05 through 2020.06.16.
33. K- and Q-band VLBI Calibrators near the Galactic Center, PI: Y. Pihlstrom; VLBA BP251; K/Q bands; 2 segments; since 2021.03.19 through 2021.04.15
34. Searching for candidate radio sources for the GAIA astrometric link (OBRS-1), (Petrov 2011); VLBA+EVN GC030; 1 segment; 2008.03.07.
35. Searching for candidate radio sources for the Gaia astrometric link and Global VLBI observations of weak sources (OBRS-2), (Petrov 2011); VLBA+EVN GC034,GB073; 7 segments; since 2010.03.23 through 2012.05.27.
36. Search for SOuthern Fermi Unassociated sources (SOFUS), PI: L. Petrov; LBA SOFUS; X-band; 2 segments; 2017.04.07 through 2017.07.10.
37. VLBI Ecliptic band survey with the CVN (VEPS-1), (Shu et al. 2017); CVN VEPS; X band; 17 segments; since 2015.02.13 through 2017.12.14.
38. Bessel Calibrator Search (BeSSel), (Immer et al. 2011); VLBA BR145; X-band; 34 segments; since 2009.11.16 through 2010.08.29.

39. Bessel Calibrator Search follow-on, PI: M. Reid; VLBA BR149; X-band; 13 segments; since 2012.08.07 through 2013.08.04.
40. The Bologna Complete Sample of Nearby Radio Sources, (Liuzzo et al. 2009); VLBA BG069, BG094, BG158; 2 segments; since 1997.04.06 through 2000.01.22.
41. Densification of the International Celestial Reference Frame, (Charlot et al. 2004); EVN EC013, EC017; S/X bands; 3 segments; since 2000.05.31 through 2003.10.17
42. A VLBA Survey of Flat-Spectrum FIRST Sources, (Ulvestad et al. 1999) VLBA BU007; C band; 1 segment; 1996.12.19
43. Caltech Jodrell Bank snapshot survey, (Britzen et al. 2007); VLBA BB119; C band; 3 segments; since 1999.11.21 through 1999.11.26.
44. LBA Calibrator Survey-1 (LCS-1), (Petrov et al. 2011b); LBA V254, V271; X band; 4 segments; since 2008.02.05 through 2009.12.12
45. LBA Calibrator Survey-2 (LCS-2), (Petrov et al. 2019); LBA V271, V441, V493; X band; 14 segments; since 2010.03.11 through 2016.06.28.

Astrometric follow-ups:

46. Regular Geodesy with VLBA (RDV), (Petrov et al. 2009), VLBA RV, RDV, BR, TC, BW, RDG, WAP, CN18, CN19; S/X bands; 189 segments, since 1994.07.08 through 2020.07.07.
47. S/X Astrometry Program, (Fey & Charlot 1997), VLBA BF025; S/X bands; 2 segments; since 1997.01.10 through 1997.01.11.
48. VLBA Ecliptic Plane Survey (VEPS-1), (Shu et al. 2017); VLBA BS250; S/X bands; 4 segments; since 2016.03.22 through 2016.05.19.
49. VLBA Ecliptic Plane Survey 2 (VEPS-2), PI: F. Shu; VLBA BS264; S/X bands; 6 segments; since 2018.03.21 through 2018.06.15.
50. VLBI Ecliptic Plane Survey followup, PI: L. Petrov; CVN VEPS-F; S/X bands; 2 segments; since 2018.01.24 through 2018.02.10.
51. Probing milliarcsecond optical structure through VLBI observations of Gaia detected AGNs, PI: L. Petrov; VLBA BP222,BP236; X/S bands; 38 segments; since 2018.05.15 through 2020.04.19.
52. Revealing milliarcsecond optical structure through VLBI observations of Gaia detected AGNs at Southern Hemisphere, PI: L. Petrov; LBA V561; S/X bands; 2 segments; since 2017.06.16 through 2018.03.14.
53. Second epoch VLBA Calibrator survey (VCS-II) (Gordon et al. 2016); VLBA BG219; S/X bands; 9 segments; since 2014.01.04 through 2015.03.17.
54. Third epoch VLBA Calibrator survey (VCS-III); PI: A. Fey; VLBA UF001; S/X bands; 20 segments; since 2017.01.16 through 2017.10.21.
55. Fourth epoch VLBA Calibrator survey (VCS-IV), PI: D. Gordon; VLBA UG002; S/X bands; 24 segments; since 2018.01.18 through 2019.01.21.
56. SOuthern Astrometry Program, PI: L. Petrov; LBA AUA; S/X bands; 24 segments; since 2017.08.22 through 2019.12.04.

High frequency extensions:

57. K-band KVN calibrator survey, PI: J. A. Lee; KVN N13JL01, S14JL01; K-band; 7 segments; since 2013.09.04 through 2014.12.24.

58. K/Q survey, (Lanyi et al. 2010; Charlot et al. 2010); VLBA BR079,BL115,BL122,BL151,BL166; X/K/Q bands; 14 segments; since 2002.05.15 through 2011.02.05.
59. UD001 K-band astrometry, PI: A. de Witt; VLBA UD001; K band; 24 segments; since 2017.01.08 through 2018.07.22.
60. Improving the K-band Celestial Reference Frame in the North; PI: A. de Witt; VLBA BJ083; K band; 5 segments; since 2015.07.21 through 2016.06.20